

Infall and rotation motions in the HH 111 protostellar system: A flattened envelope in transition to a disk?

Chin-Fei Lee^{1,2}, Yao-Yuan Mao³, Bo Reipurth⁴

ABSTRACT

We have mapped the central region of the HH 111 protostellar system in 1.33 mm continuum, C¹⁸O (J=2-1), ¹³CO (J=2-1), and SO ($N_J = 5_6 - 4_5$) emission at $\sim 3''$ resolution with the Submillimeter Array. There are two sources, VLA 1 (=IRAS 05491+0247) and VLA 2, with the VLA 1 source driving the HH 111 jet. Thermal emission is seen in 1.33 mm continuum tracing the dust in the envelope and the putative disks around the sources. A flattened, torus-like envelope is seen in C¹⁸O and ¹³CO around the VLA 1 source surrounding the dust lane perpendicular to the jet axis, with an inner radius of ~ 400 AU ($1''$), an outer radius of ~ 3200 AU ($8''$), and a thickness of ~ 1000 AU ($2''.5$). It seems to be infalling toward the center with conservation of specific angular momentum rather than with a Keplerian rotation as assumed by Yang et al. (1997). An inner envelope is seen in SO, with a radius of ~ 500 AU ($1''.3$). The inner part of this inner envelope, which is spatially coincident with the dust lane, seems to have a differential rotation and thus may have formed a rotationally supported disk. The outer part of this inner envelope, however, may have a rotation velocity decreasing toward the center and thus represent a region where an infalling envelope is in transition to a rotationally supported disk. A brief comparison with a collapsing model suggests that the flattened, torus-like envelope seen in C¹⁸O and ¹³CO could result from a collapse of a magnetized rotating toroid.

Subject headings: stars: formation — ISM: individual: HH 111 — ISM: circumstellar matter.

¹Academia Sinica Institute of Astronomy and Astrophysics, P.O. Box 23-141, Taipei 106, Taiwan; cflee@asiaa.sinica.edu.tw

²Harvard-Smithsonian Center for Astrophysics, Submillimeter Array, 645 North A'ohoku, Hilo, HI 96720

³Department of Physics, National Taiwan University, Taipei 10617, Taiwan

⁴Institute for Astronomy, University of Hawaii, Hilo, HI, USA

1. Introduction

Stars are formed inside molecular cloud cores by means of gravitational collapse. The details of the process, however, are complicated by the presence of magnetic fields and angular momentum. As a result, in addition to infall (or collapse), rotation and outflow are also seen toward star-forming regions. In theory, a rotationally supported disk is expected to form inside a collapsing core around a protostar, from which part of the material is accreted by the protostar and part is ejected away. Observationally, however, when and how a rotationally supported disk is actually formed are still unclear, because of the lack of detailed kinematic studies inside the collapsing core.

A rotationally supported disk has been seen with a radius of ~ 500 AU in the late (i.e., Class II or T Tauri) phase of star formation (see, e.g., Simon et al. 2000). Formation of such a disk must have started early in the Class 0 phase. However, no such disk has been confirmed in the Class 0 phase, probably because it is still too small (< 100 AU) for a detailed kinematic study with current instruments (see, e.g., Lee et al. 2006; Jørgensen et al. 2007). In order to investigate how a rotationally supported disk is formed inside a collapsing core, we have mapped the protostellar system HH 111, which is in the Class I phase and is thus expected to have a bigger disk than that in the Class 0 phase. In this system, a Class I source IRAS 05491+0247 is found deeply embedded in a compact molecular cloud core in the L1617 cloud of Orion, driving the HH 111 jet (Reipurth 1989). The distance to the Orion Nebula Cluster has been recently refined to be 400 pc (Sandstrom et al. 2007; Menten et al. 2007), the same that is generally adopted for the Orion B cloud (see, e.g., Gibb 2008) with which L1617 is associated. The HH 111 system has traditionally been assumed to be at a distance of 450 pc, but we here adopt this new distance, at which the source has a luminosity of $\sim 20 L_{\odot}$ (Reipurth 1989). A rotating envelope has been seen around the source inside the core (Stapelfeldt & Scoville 1993) and may have infall motion toward the source (Yang et al. 1997). The jet complex is highly collimated with a two-sided length of ~ 6.7 pc (Reipurth, Bally, & Devine 1997, corrected for the new distance), and it produces a collimated molecular outflow around it (Nagar et al. 1997; Lee et al. 2000). The source has also been detected with the VLA, associated with a tiny radio jet (Reipurth et al. 1999), and a tiny dusty disk (with a radius of 30 AU) (Rodríguez et al. 2008) that can be the innermost part of a rotationally supported disk. Thus, this system is one of the best candidates to search for a rotationally supported disk and investigate how it is formed inside a collapsing core. Here, we present observations of the envelope in 1.33 mm continuum, $^{13}\text{CO}(J = 2 - 1)$, $\text{C}^{18}\text{O}(J = 2 - 1)$, and $\text{SO}(N_J = 5_6 - 4_5)$ emission obtained with the Submillimeter Array

(SMA)¹ (Ho et al. 2004).

2. Observations

Observations toward the protostellar system HH 111 were carried out with the SMA on 2005 December 5 in the compact-north configuration using the 230 GHz band receivers. The receivers have two sidebands, lower and upper. With the local oscillator (LO) frequency set to 224.677 GHz, we observed the $^{12}\text{CO}(J = 2 - 1)$ line in the upper sideband, the $^{13}\text{CO}(J = 2 - 1)$, $\text{C}^{18}\text{O}(J = 2 - 1)$, and $\text{SO}(N_J = 5_6 - 4_5)$ lines in the lower sideband simultaneously. The ^{12}CO line traces mainly the outflow interaction and will be presented in a future publication. Combining the line-free portions of the two sidebands results in a total continuum bandwidth of ~ 3.9 GHz centered at the LO frequency (or $\lambda \sim 1.33$ mm) for the continuum. Seven antennas were used, giving baselines with projected lengths ranging from 8 to 53 m. The correlator was set up to give a velocity resolution of 0.28 km s^{-1} per channel for the ^{12}CO , ^{13}CO , and C^{18}O lines, and 0.56 km s^{-1} per channel for the SO line. Three pointings with a separation of $\sim 28''$ were used to map the envelope and the outflow lobe extending to the west. Here, we only present the envelope region close to the source.

The visibility data were calibrated with the MIR package, with Uranus as a flux calibrator, quasar 3c454.3 as a passband calibrator, and quasar 0530+135 as a gain calibrator. The flux uncertainty is estimated to be $\sim 15\%$. The calibrated visibility data were imaged with the MIRIAD package. The dirty maps that were produced from the calibrated visibility data were CLEANed using the Steer clean method, producing the CLEAN component maps. The final maps were obtained by restoring the CLEAN component maps with a synthesized (Gaussian) beam fitted to the main lobe of the dirty beam. With natural weighting, the synthesized beam has a size of $3''.5 \times 3''.2$ at a position angle (P.A.) of $\sim -50^\circ$. The rms noise levels are $\sim 0.22 \text{ Jy beam}^{-1}$ in the ^{13}CO and C^{18}O channel maps, $0.15 \text{ Jy beam}^{-1}$ in the SO channel maps, and $3.5 \text{ mJy beam}^{-1}$ in the continuum map. The velocities of the channel maps are LSR.

¹The Submillimeter Array is a joint project between the Smithsonian Astrophysical Observatory and the Academia Sinica Institute of Astronomy and Astrophysics, and is funded by the Smithsonian Institution and the Academia Sinica.

3. Results

Our results are presented in comparison to a mosaic image based on the Hubble Space Telescope (HST) NICMOS images ([FeII] 1.64 μm + H₂ at 2.12 μm + continuum) obtained by Reipurth et al. (1999), which shows clear detection of two infrared sources, reflection nebulae tracing the illuminated outflow cavity walls, and the jet in the system. The two infrared sources are named stars A and B, with star A being the IRAS source. They are also detected in 3.6 cm continuum by the VLA as the VLA 1 and 2 sources, respectively, at $\alpha_{(2000)} = 05^{\text{h}}51^{\text{m}}46^{\text{s}}.25$, $\delta_{(2000)} = +02^{\circ}48'29''.5$ and $\alpha_{(2000)} = 05^{\text{h}}51^{\text{m}}46^{\text{s}}.07$, $\delta_{(2000)} = +02^{\circ}48'30''.6$ (Reipurth et al. 1999). These VLA positions, which are more accurate than the NICMOS positions, are adopted here as the source positions. In this region, the systemic velocity is assumed to be given by the line peak of the optically thin SO emission, which is $8.84 \pm 0.28 \text{ km s}^{-1}$ LSR. Note that this value is higher than that derived from the ¹³CO emission averaged over a much larger region by Reipurth & Olberg (1991), which was 8.5 km s^{-1} . Throughout this paper, the velocity is relative to this systemic value.

3.1. Continuum Emission

A compact continuum emission is detected at 1.33 mm, with an emission peak well coincident with the VLA 1 position (Fig. 1a). It has a total flux of 280 ± 40 mJy, about 60% of that measured for a much larger region in the single-dish observation (Reipurth et al. 1993). The emission is spatially unresolved, mainly arising from around the VLA 1 source. Some faint emission is also seen extending towards the VLA 2 source. From the spectral energy distribution (SED) (Fig. 1b), it is clear that the emission at 1.33 mm is thermal emission from the dust in the envelope and the putative disks around the VLA 1 and 2 sources (Reipurth et al. 1999; Rodríguez et al. 2008). Assuming that the mass opacity is given by

$$\kappa_{\nu} = 0.1 \left(\frac{\nu}{10^{12} \text{Hz}} \right)^{\beta} \text{ cm}^2 \text{ g}^{-1} \quad (1)$$

the SED between $\lambda = 3.06 \text{ mm}$ and $25 \mu\text{m}$ can be fitted with $\beta \simeq 0.9$ and a dust temperature of 41–64 K. With these fits, the emission is found to be optically thin at 1.33 mm. The total mass of the gas and dust associated with the envelope and the putative disks is estimated to be $\sim 0.15\text{--}0.09 M_{\odot}$.

3.2. Line Emission

Unlike the continuum emission, C^{18}O , ^{13}CO , and SO emission are all seen with a peak near the center of the dark ridge (i.e., the dust lane) seen in the HST image, which is $\sim 0''.5$ to the west of the VLA 1 source (Fig. 2). The C^{18}O emission shows similar structures to those seen in CS (Yang et al. 1997). It shows a north-south elongation roughly perpendicular to the jet axis, tracing a flattened envelope around the VLA 1 source. The C^{18}O emission also extends slightly to the west along the jet axis and southwest along the outflow cavity wall outlined by the reflection nebulae. The ^{13}CO emission is more extended, tracing both the envelope and the outflow cavity walls. The SO emission is more compact with a narrow waist around the source. It also extends along the outflow cavity walls in the southeast, southwest, and northwest directions.

The dark ridge, where the line emissions all peak, has been suggested to be the birthplace of both the VLA 1 and 2 sources (Reipurth et al. 1999) and thus can be assumed to be the center of the flattened envelope. The C^{18}O , ^{13}CO , and SO spectra toward the dark ridge all show a similar FWZI of $\sim 6 \text{ km s}^{-1}$ (Fig. 3). The SO spectrum is rather symmetric with a single peak at the systemic velocity. The C^{18}O and ^{13}CO spectra show a double-peaked profile with a dip coincident with the SO peak, and with the blueshifted peak brighter than the redshifted peak (i.e., the blue asymmetry). Comparing to the single-dish observations toward a larger region, we find that there is missing flux in ^{13}CO and C^{18}O within $\sim 1 \text{ km s}^{-1}$ of the systemic velocity as the large-scale flux is resolved out in our interferometric observation (Fig. 4). Note that, however, since missing flux tends to produce a dip with similar redshifted peak and blueshifted peak, an additional mechanism is still needed to produce the observed dips with the blue asymmetry. It could be self-absorption due to an infall motion in the envelope (see, e.g., Evans 1999). Infall motion has already been suggested by Yang et al. (1997) using CS observations. The ^{13}CO emission is optically thicker and thus shows a deeper and wider absorbing dip than the C^{18}O emission. The SO emission does not show a dip, likely because it is optically thin due to low SO abundance.

In order to show the kinematics of the flattened envelope, the emission is divided into four velocity components: low redshifted and blueshifted emission with velocity within $\sim 1 \text{ km s}^{-1}$ from the systemic, and high redshifted and blueshifted emission with velocity higher than 1 km s^{-1} from the systemic (Fig. 2). At low velocity, the C^{18}O emission clearly shows a flattened structure with the blueshifted and redshifted emission extended $\sim 7''$ (2800 AU) to the north and south, respectively, from the dark ridge, as expected for a rotating envelope. The redshifted emission fits right in between the eastern and western reflection nebulae in the south. This is to be expected since the reflection nebulae trace the regions with less extinction and thus low density in the boundary of the envelope. Therefore, with

the boundary defined by those reflection nebulae, the envelope is found to have a thickness of $\sim 2''.5$ (i.e., 1000 AU) and roughly constant with increasing distance from the source. Note that the blueshifted emission also traces the outflow emission in the west and the outflow cavity wall in the southwest. At high velocity, the emission shrinks toward to the source, arising from the inner part of the envelope. The blueshifted peak shifts slightly to the west and the redshifted peak slightly to the east. These shifts further suggest an infall motion in the envelope, with the blueshifted peak in the far end (west) of the envelope and the redshifted peak in the near end (east), as suggested in Yang et al. (1997). These shifts are also partly due to an outflow component, with the emission extended to the west and along the cavity walls. In ^{13}CO , the blueshifted emission peaks to the northwest and redshifted emission in the southeast of the dark ridge even at low velocity. As seen in the spectrum, the lowest-velocity ^{13}CO emission, which traces the flattened envelope further out, is missing more than the C^{18}O emission, and thus revealing the inner part of the envelope, where the radial motion becomes prominent. In SO , the blueshifted and redshifted emission are also seen to the northwest and southwest of the dark ridge, similar to that seen in ^{13}CO . The SO emission is likely optically thin, probing directly the inner part of the envelope.

4. A simple model for the envelope

4.1. Velocity structure of the envelope

The rotational velocity of the flattened envelope can be studied with the position-velocity (PV) diagrams centered at the dark ridge cut perpendicular to the jet axis. The ^{13}CO and C^{18}O emission show similar kinematics (Figs. 5a, b) and can be studied together. The blueshifted emission is seen mainly to the north and redshifted emission mainly to the south, confirming a rotation in the envelope. At low velocity, the blueshifted and redshifted emissions also extend across the center to the south and north, respectively, suggesting that there is also a radial motion in the envelope. The rotational velocity is seen increasing toward the center and thus could be Keplerian or that conserving specific angular momentum. In the case of Keplerian rotation, the best fit to the velocity structures in these two line emissions together is $v_\phi = 1.3(R/R_0)^{-1/2}$ km s $^{-1}$ with $R_0 = 400$ AU (i.e., $1''$), which is slightly faster than that found in CS at lower angular resolution by Yang et al. (1997). This Keplerian rotation corresponds to a stellar mass of $\sim 0.8 M_\odot$. Here, the plane of the flattened envelope is assumed to have an inclination of 10° away from the line of sight (Reipurth, Raga, & Heathcote 1992). In the case of conservation of specific angular momentum, the best fit is $v_\phi = 1.6(R/R_0)^{-1}$ km s $^{-1}$. With a reduced $\chi^2 = 0.07$, it seems to fit better than the Keplerian rotation, which has a reduced $\chi^2 = 0.11$ and decreases too fast

toward the center as compared with the observed. To confirm it, however, both observations at higher angular resolution and shorter uv spacings are needed. The latter is to retrieve the missing flux at low velocity. The SO emission traces only the inner part of the envelope. Its velocity structure is not well resolved and seems to have two components: a low-velocity component in the inner part with the velocity within $\sim 1.5 \text{ km s}^{-1}$ of the systemic, and a high-velocity component in the outer part with the velocity higher than $\sim 1.5 \text{ km s}^{-1}$ (Fig. 5c). The low-velocity component seems to have a radius of $\sim 0''.5$ (200 AU) and a differential rotation with the velocity increasing toward the center. The high-velocity component extends to $R \sim 1.3''$ ($\sim 500 \text{ AU}$), connecting to that of the ^{13}CO emission. Its velocity, however, seems to increase with increasing distance from the center. It could arise from a solid-body (rigid) rotation with $v_\phi = 2.0(R/R_0) \text{ km s}^{-1}$. It could also arise from an outflow motion.

The radial motion in the envelope can be studied with the PV diagrams cut along the jet axis (Figs. 5d, e, f). The PV diagrams, however, are highly contaminated by the outflow emission, especially on the blueshifted side. Only part of the emission close to the center to within e.g., $2''$ (which corresponds to a deprojected distance of $\sim 10''$ at an inclination of $\sim 10^\circ$) is believed to be from the envelope. The C^{18}O , ^{13}CO , and SO emission within $\sim 2''$ from the center seem to show similar velocity structure. The blueshifted emission is mainly in the west and the redshifted emission is mainly in the east. On the redshifted side, where the outflow contamination is less, the velocity seems to increase toward the center. This velocity structure is unlikely due to an outflow motion for which the velocity is expected to decrease toward the center (see, e.g, Lee et al. 2001). It could arise from an infall motion in the envelope, as suggested. For a dynamical collapse, the infall motion can be assumed to be a free-fall motion as in Yang et al. (1997), with the infall velocity $v_r = -v_{r0}(R/R_0)^{-1/2}$. Three values of v_{r0} , 2.4, 1.9, and 1.5, are compared to the C^{18}O , ^{13}CO , and SO velocity structures, with the second value corresponding to that obtained by Yang et al. (1997). The corresponding stellar masses are 1.3, 0.8, 0.5 M_\odot , respectively. The one with the least mass seems to give the best fit, matching the emission at the lowest velocity in the redshifted part where the contamination of the outflow emission is less. However, observation at higher angular resolution is really needed to confirm it.

4.2. Density structure of the envelope

In order to obtain roughly the density distribution of the flattened envelope, a simple disklike envelope model as described in Lee et al. (2006) is compared to the C^{18}O emission, which suffers less missing flux than the ^{13}CO emission. In this model, the envelope has a

free-fall motion and a rotation with conservation of specific angular momentum, with the best-fit parameters given above. It has an inner radius of R_{in} , an outer radius of R_{out} , and a constant thickness of H , in cylindrical coordinates. The number density of molecular hydrogen is assumed to be given by

$$n = n_0 \left(\frac{R}{R_0} \right)^p \quad (2)$$

where n_0 is the density at R_0 and p is a power-law index assumed to be -1.5 , as in many theoretical infalling models (see, e.g., Shu 1977; Nakamura 2000). The temperature of the envelope is uncertain and assumed to be given by

$$T = T_0 \left(\frac{R}{R_0} \right)^q \quad (3)$$

where T_0 is the temperature at R_0 and q is a power-law index. The abundance of C^{18}O relative to molecular hydrogen is assumed to be constant and given by 1.7×10^{-7} (Frerking et al. 1982). In the model calculations, radiative transfer is used to calculate the emission, with an assumption of local thermal equilibrium. For simplicity, the line width is assumed to be given by the thermal line width only. The channel maps of the emission derived from the model are convolved with the observed beam and velocity resolution, and then used to make the integrated map, spectrum, and PV diagram.

There are six parameters in this model: R_{in} , R_{out} , H , n_0 , T_0 , and q . In our fits, we have $R_{\text{in}} \sim 400$ AU ($\sim 1''$), $R_{\text{out}} \sim 3200$ AU ($\sim 8''$), $H \sim 1000$ AU (i.e., $2''.5$), $n_0 \sim 9 \times 10^6$ cm^{-3} , $T_0 \sim 40$ K, and $q \sim -0.6$. Here T_0 is assumed to be the lower end of the dust temperature. As can be seen in Fig. 6, this model can roughly reproduce the envelope structure, spectrum, and PV diagram of the C^{18}O emission, except for the emission at high-redshifted velocity. The position of the two peaks in the line profile can also be roughly matched with the assumed infall velocity. Note that, however, the temperature power-law index is required to be steeper here in order to reproduce the observed dip at the systemic velocity, as compared to those ($q \sim -0.4$) obtained by fitting other envelopes in single-dish observations (see, e.g., Hogerheijde 2001). It could be because the dip is partly due to the missing flux of the large-scale gas and the absorption by this large-scale gas as well.

The mass of the flattened envelope, which is given by

$$M_e = 2m_{\text{H}}n_0H \int_{R_{\text{in}}}^{R_{\text{out}}} \left(\frac{R}{R_0} \right)^{-1.5} 2\pi R dR \quad (4)$$

is $\sim 0.2 M_{\odot}$, consistent with that found by Stapelfeldt & Scoville (1993). This mass is higher than that derived from the continuum emission, which is more compact. In our simple model,

the infall rate, which is given by

$$\begin{aligned} \dot{M}(R) &= 2\pi R H n |v_R| \cdot 2m_{\text{H}} \\ &\approx 4 \times 10^{-5} \left(\frac{R}{R_0}\right)^{-1} M_{\odot} \text{ yr}^{-1} \end{aligned} \quad (5)$$

has a mean value of $\sim 10^{-5} M_{\odot} \text{ yr}^{-1}$, averaged over the radius. The accretion rate, if assumed to be the mean infall rate, would result in an accretion luminosity of $L_{\text{acc}} = GM_* \dot{M}_{\text{acc}} / R_* \sim 37 L_{\odot}$, assuming a stellar mass of $M_* \sim 0.5 M_{\odot}$ (as derived from the infall velocity) and a stellar radius of $R_* \sim 4R_{\odot}$. This luminosity, however, is about twice the luminosity of the source, which is $\sim 20 L_{\odot}$ (Reipurth 1989). In addition, the accretion time would be only $\sim 5 \times 10^4$ yr for forming a source with a mass of $0.5 M_{\odot}$, shorter than that for a typical Class I source. Thus, the accretion rate could be smaller than the infall rate.

4.3. Summary - A Collapsing torus

The envelope seen in C^{18}O and ^{13}CO can be considered as a thick torus around the narrow dust lane (i.e., the dark ridge), with an inner radius of 400 AU ($1''$), an outer radius of 3200 AU ($8''$), and a thickness of 1000 AU ($2''.5$). It has a differential rotation that seems to be better fitted by a rotation with conservation of specific angular momentum than by a Keplerian rotation as assumed by Yang et al. (1997). The envelope likely also has an infall motion, with the blueshifted emission in the far end and the redshifted emission in the near end, showing a double-peaked line profile with a blue asymmetry and an absorption dip at the systemic velocity. Therefore, the envelope seems to be infalling (contracting) toward the center preserving its angular momentum, similar to other infalling envelopes in the Class I phase (Ohashi et al. 1997; Momose et al. 1998; Lee & Ho 2005) and even in the Class 0 phase (e.g., Lee et al. 2005). With the derived rotation and infall velocity structures, the rotation velocity is equal to the infall velocity at $R \sim 1''.5$ (600 AU), suggesting that the centrifugal force starts to dominate in the inner edge of the envelope.

5. Discussion

5.1. Magnetic braking and SO disk?

The inner envelope is seen in SO as in HH 212 (Lee et al. 2006). It has an outer radius similar to where the centrifugal force starts to dominate. Therefore, a rotationally supported disk is expected to form here. Such a disk may indeed have formed in the inner part of this

inner envelope, which is seen with a differential rotation, spatially coincident with the narrow dark ridge that could be interpreted as a dense circumstellar disk (Reipurth et al. 1999). The outer part of this inner envelope, however, may have a rotation velocity decreasing toward the center. If this is the case, the angular momentum might have been efficiently removed from there. This can be achieved with the presence of a magnetic field. It has been found that a magnetic field can enforce solid-body rotation because magnetic braking can eliminate differential rotation on a timescale much shorter than even the free-fall timescale (Mouschovias & Ciolek 1999).

5.2. Comparing with a Theoretical Model

Currently, the most popular model of star formation is Shu’s model (derived from Shu 1977). One recent version of this model assumes the collapse of a magnetized singular isothermal rotating toroid (Allen, Li, & Shu 2003; Mellon & Li 2008). In this model, a pseudodisk (a nonrotationally supported thick torus) is formed around the source. In the inner edge of the pseudodisk, the rotation speed drops steadily with decreasing radius, as a result of efficient braking by the strong magnetic field.

In our observations, it is possible that the flattened envelope seen in $C^{18}O$ and ^{13}CO is a pseudodisk resulting from the collapse of a magnetized rotating toroid toward the center. It is also possible that the outer part of the SO envelope is the inner edge of the pseudodisk where the rotation velocity decreases with decreasing radius due to efficient magnetic braking. However, further observations are really needed to confirm the rotation velocity structure in the flattened envelope and to tell whether the structure of the infalling material is magnetically-guided. In addition, a slow outflow, which is expected when there is a twisting of magnetic field lines (Allen, Li, & Shu 2003), has not yet been identified in our observations.

In their model, a rotationally supported disk is not able to form around the source due to the efficient loss of angular momentum (Allen, Li, & Shu 2003; Mellon & Li 2008). In the HH 111 system, such a disk must have already formed around the source to launch the jet. In addition, the innermost part of the disk has been seen as a tiny dusty disk (with a radius of 30 AU) around the source (Rodríguez et al. 2008). As suggested by Shu et al. (2006), one possibility is to have an ohmic resistivity in the model, so that the magnetic field can be dissipated efficiently around the source.

5.3. Gas depletion?

The continuum emission peaks at the VLA 1 position while the line emissions all peak around the dark ridge, suggesting that the dust and gas peak at different positions. It could be because there is a lack of gas toward the continuum peak. It has been suggested by Reipurth et al. (1999) that the VLA 1 and VLA 2 sources were originally formed in the dark ridge inside the envelope but later ejected from there. Thus, the continuum emission peak could trace the inner disk carried away by the VLA 1 source, as suggested in Reipurth et al. (1999). If this is the case, there could be a lack of gas (depletion) toward the inner disk.

6. Conclusion

We have mapped the central region of the protostellar system HH 111 in 1.33 mm continuum, $C^{18}O$ ($J=2-1$), ^{13}CO ($J=2-1$), and SO ($N_J = 5_6 - 4_5$) emission at $\sim 3''$ resolution with the Submillimeter Array. There are two sources, VLA 1 (=IRAS 05491+0247) and VLA 2, with the VLA 1 source driving the HH 111 jet. Thermal emission is seen in 1.33 mm continuum tracing the dust in the envelope and the putative disks around the sources. A flattened, torus-like envelope is seen in $C^{18}O$ and ^{13}CO around the VLA 1 source surrounding the dust lane perpendicular to the jet axis, with an inner radius of ~ 400 AU ($1''$), an outer radius of ~ 3200 AU ($8''$), and a thickness of ~ 1000 AU ($2''.5$). It seems to be infalling toward the center with conservation of specific angular momentum rather than with a Keplerian rotation as assumed by Yang et al. (1997). An inner envelope is seen in SO , with a radius of ~ 500 AU ($1''.3$). The inner part of this inner envelope, which is spatially coincident with the dust lane, seems to have a differential rotation and thus may have formed a rotationally supported disk. The outer part of this inner envelope, however, may have a rotation velocity decreasing toward the center and thus represent a region where an infalling envelope is in transition to a rotationally supported disk. A brief comparison with a collapsing model suggests that the flattened, torus-like envelope seen in $C^{18}O$ and ^{13}CO could be a pseudodisk (a nonrotationally supported torus) resulting from a collapse of a magnetized rotating toroid.

We thank the SMA staff for their efforts in running and maintaining the array. We also thank the referee, Dan Watson, for his valuable comments. BR is partly supported by the NASA Astrobiology Institute under Cooperative Agreement No. NNA04CC08A issued through the Office of Space Science.

REFERENCES

- Allen, A., Li, Z., & Shu, F. H. 2003, *ApJ*, 599, 363
- Cernicharo, J., & Reipurth, B. 1996, *ApJ*, 460, L57
- Evans, N. J., II 1999, *ARA&A*, 37, 311
- Frerking, M. A., Langer, W. D., & Wilson, R. W. 1982, *ApJ*, 262, 590
- Gibb, A.G. 2008, in *Handbook of Star Forming Regions*, Ed. Bo Reipurth, Astron. Soc. Pacific, in press
- Ho, P. T. P., Moran, J. M., & Lo, K. Y. 2004, *ApJ*, 616, L1
- Hogerheijde, M. R. 2001, *ApJ*, 553, 618
- Jørgensen, J. K., et al. 2007, *ApJ*, 659, 479
- Lee, C.-F., Ho, P. T. P., Beuther, H., Bourke, T. L., Zhang, Q., Hirano, N., & Shang, H. 2006, *ApJ*, 639, 292
- Lee, C.-F., Mundy, L. G., Reipurth, B., Ostriker, E. C., & Stone, J. M. 2000, *ApJ*, 542, 925
- Lee, C.-F., Stone, J. M., Ostriker, E. C., & Mundy, L. G. 2001, *ApJ*, 557, 429
- Lee, C.-F., & Ho, P. T. P. 2005, *ApJ*, 632, 964
- Lee, C.-F., Ho, P. T. P., & White, S. M. 2005, *ApJ*, 619, 948
- Mellon, R. R., & Li, Z.-Y. 2008, *ApJ*, 681, 1356
- Menten, K. M., Reid, M. J., Forbrich, J., & Brunthaler, A. 2007, *A&A*, 474, 515
- Momose, M., Ohashi, N., Kawabe, R., Nakano, T., & Hayashi, M. 1998, *ApJ*, 504, 314
- Mouschovias, T. C. & Ciolek, G. E. 1999, *NATO ASIC Proc. 540: The Origin of Stars and Planetary Systems*, 305
- Nagar, N. M., Vogel, S. N., Stone, J. M., & Ostriker, E. C. 1997, *ApJ*, 482, L195
- Nakamura, F. 2000, *ApJ*, 543, 291
- Ohashi, N., Hayashi, M., Ho, P. T. P., Momose, M., Tamura, M., Hirano, N., & Sargent, A. I. 1997, *ApJ*, 488, 317

- Reipurth, B., Chini, R., Krugel, E., Kreysa, E., & Sievers, A. 1993, *A&A*, 273, 221
- Reipurth, B. 1989, *Nature*, 340, 42
- Reipurth, B., Bally, J., & Devine, D. 1997, *AJ*, 114, 2708
- Reipurth, B., & Olberg, M. 1991, *A&A*, 246, 535
- Reipurth, B., Raga, A. C., & Heathcote, S. 1992, *ApJ*, 392, 145
- Reipurth, B., Yu, K. C., Rodríguez, L. F., Heathcote, S., & Bally, J. 1999, *A&A*, 352, L83
- Rodríguez, L. F., Torrelles, J. M., Anglada, G., & Reipurth, B. 2008, *AJ*, 136, 1852
- Sandstrom, K. M., Peek, J. E. G., Bower, G. C., Bolatto, A. D., & Plambeck, R. L. 2007, *ApJ*, 667, 1161
- Shu, F. H., Galli, D., Lizano, S., & Cai, M. 2006, *ApJ*, 647, 382
- Simon, M., Dutrey, A., & Guilloteau, S. 2000, *ApJ*, 545, 1034
- Stapelfeldt, K. R., & Scoville, N. Z. 1993, *ApJ*, 408, 239
- Shu, F. H. 1977, *ApJ*, 214, 488
- Yang, J., Ohashi, N., Yan, J., Liu, C., Kaifu, N., & Kimura, H. 1997, *ApJ*, 475, 683

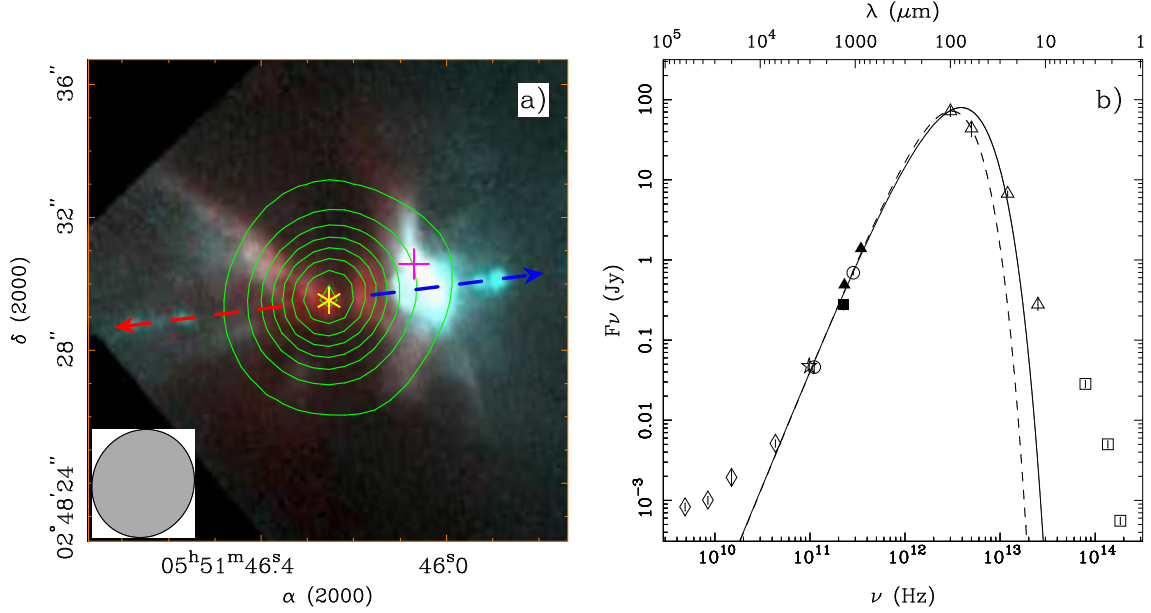


Fig. 1.— (a) The continuum emission overlotted on the HST NICMOS image from Reipurth et al. (1999). The asterisk marks the position of the IRAS source (= star A = VLA 1) and the cross marks the position of star B (= VLA 2). The contours go from 4 to 74 σ with a step of 10 σ , where $\sigma = 3.5 \text{ mJy beam}^{-1}$. The blue and red arrows indicate the orientations of the blueshifted and redshifted parts of the jet, respectively. (b) SED toward the central region. The filled square is from our observation. The diamonds are from Rodríguez et al. (2008), the star from Yang et al. (1997), the open circles from Stapelfeldt & Scoville (1993), the filled triangles from Reipurth et al. (1993), the open triangles from the IRAS catalogue, and the open squares from Reipurth & Olberg (1991). The dashed and solid lines indicate the fits with a dust temperature of 41 K and 65 K, respectively.

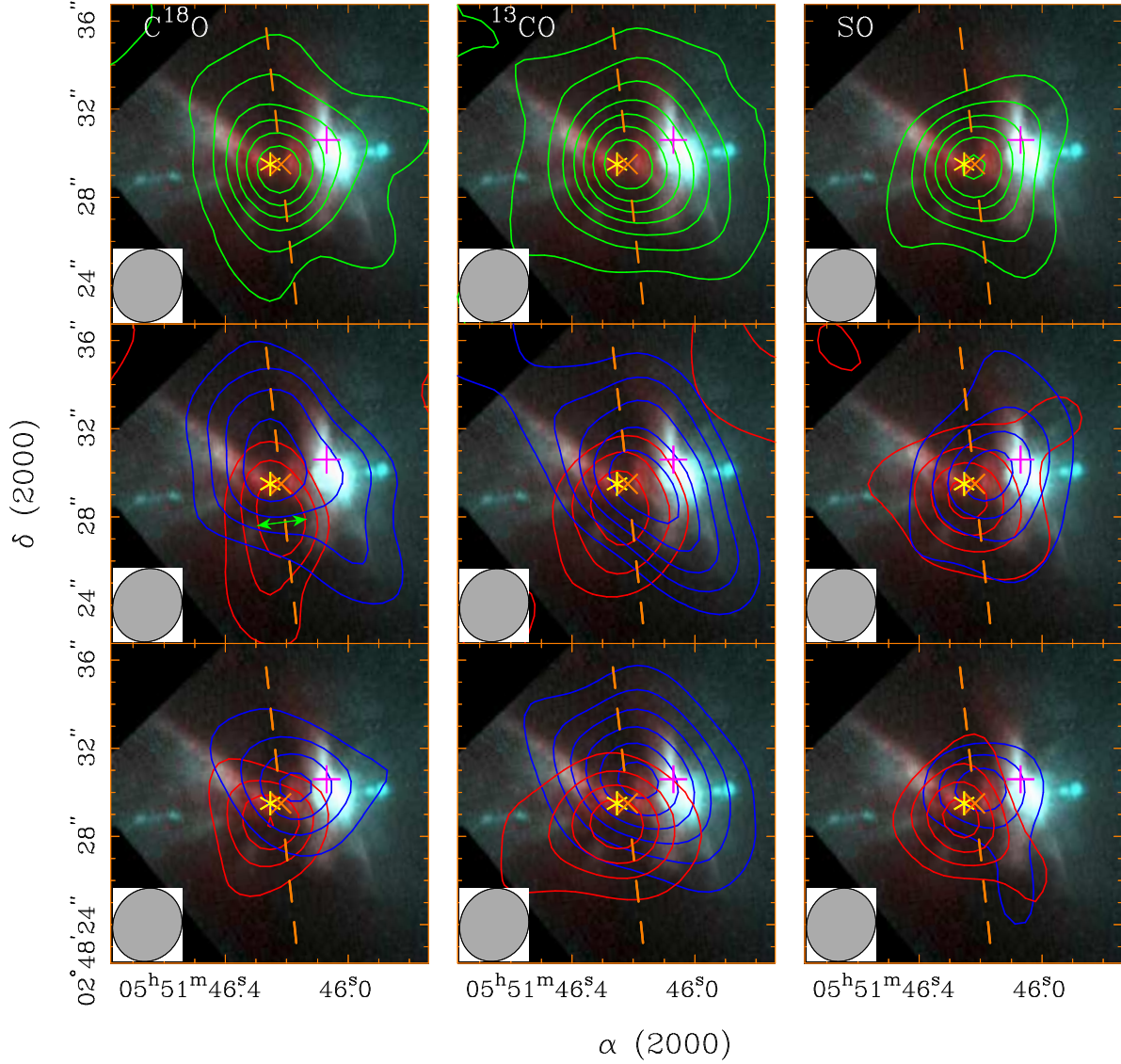


Fig. 2.— $C^{18}O$ (first column), ^{13}CO (second column), and SO (third column) emission contours on the HST NICMOS image. The asterisk marks the position of the IRAS source (= star A = VLA 1) and the cross marks the position of star B (= VLA 2). "x" marks the central position of the dark ridge and the dashed line indicates the equatorial plane perpendicular to the jet axis. (*Top row*) Total emission integrated from ~ -3 to 3 km s^{-1} . The contours go from 3 to 18σ with a step of 3σ for $C^{18}O$, from 5 to 47σ with a step of 7σ for ^{13}CO , and from 3 to 24σ with a step of 4σ for SO , where $\sigma = 0.3 \text{ Jy beam}^{-1} \text{ km s}^{-1}$. (*Middle row*) Low blueshifted and redshifted emission integrated from ~ -1 to 0 km s^{-1} and from 0 to 1 km s^{-1} , respectively. The contours go from 3 to 12σ with a step of 3σ for $C^{18}O$, from 5 to 29σ with a step of 6σ for ^{13}CO , and from 3 to 21σ with a step of 6σ for SO , where $\sigma = 0.11 \text{ Jy beam}^{-1} \text{ km s}^{-1}$. (*Bottom row*) High blueshifted and redshifted emission integrated from ~ -3 to -1 km s^{-1} and from 1 to 3 km s^{-1} , respectively. The contours go from 3 to 12σ with a step of 3σ for $C^{18}O$, from 5 to 40σ with a step of 7σ for ^{13}CO , and from 2 to 8σ with a step of 2σ for SO , where $\sigma = 0.16 \text{ Jy beam}^{-1} \text{ km s}^{-1}$.

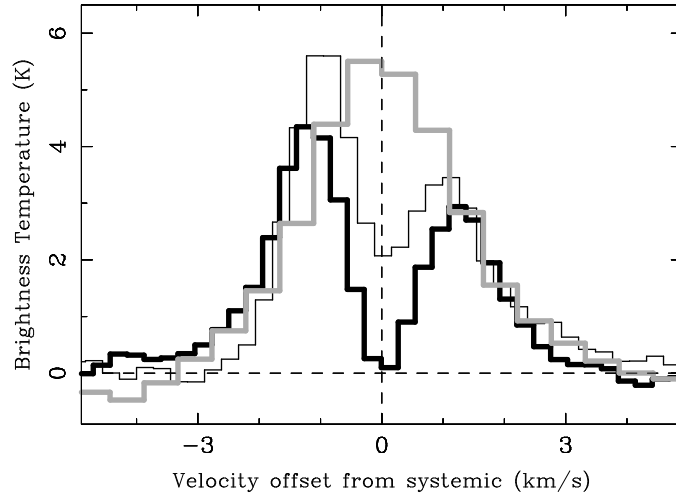


Fig. 3.— C^{18}O (thin black), ^{13}CO (thick black), and SO (thick gray) spectra toward the dark ridge seen in the NICMOS image. The ^{13}CO spectrum has been multiplied by a factor of 0.3.

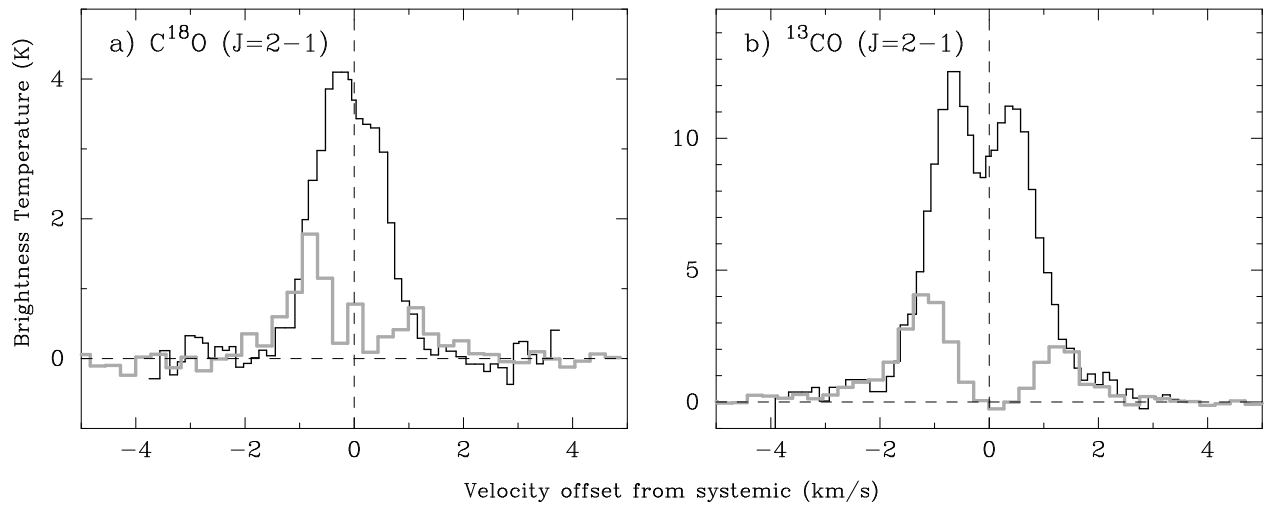


Fig. 4.— Comparison of our C^{18}O and ^{13}CO spectra (in gray) with those obtained with the IRAM 30 m telescope (in black) (Cernicharo & Reipurth 1996).

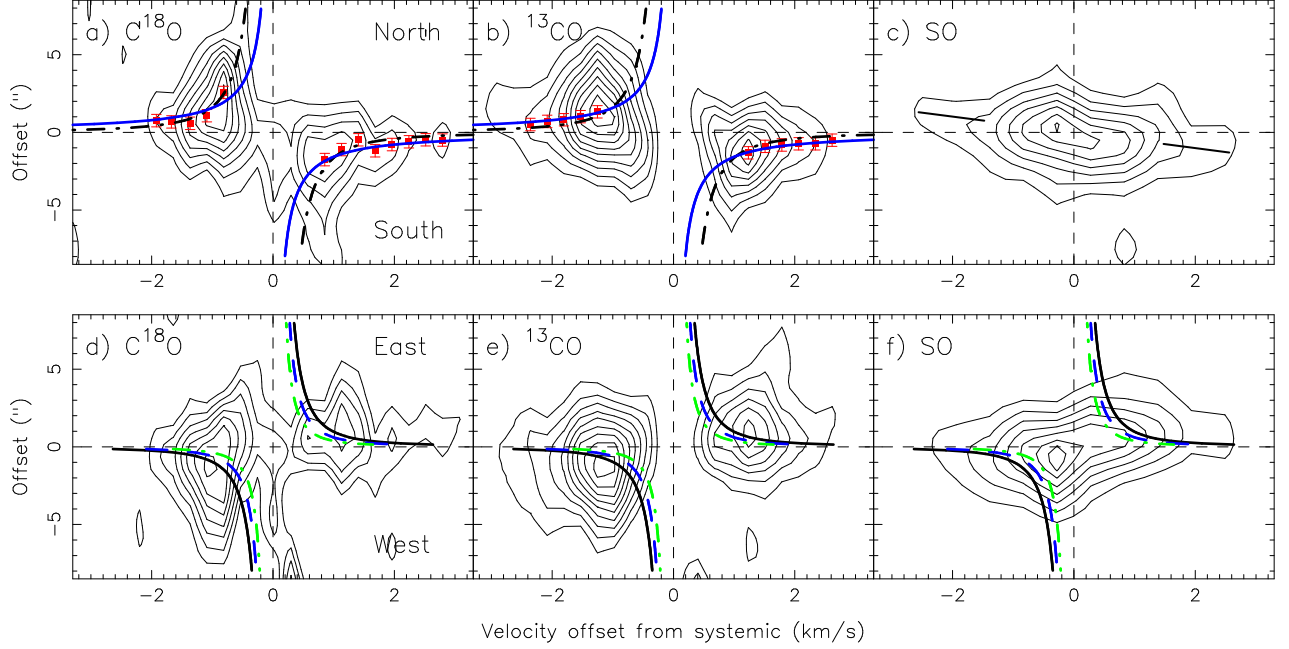


Fig. 5.— Position-velocity (PV) diagrams centered at the dark ridge. (*Top row*) PV cuts perpendicular to the jet axis. In (a) and (b), the dots with error bars represent the peak positions determined at each velocity channel. Solid curves are derived from the rotation with conservation of specific angular momentum. Dashed curves are derived from the Keplerian rotation. In (c), the solid lines are from the linear fit to the outer part of the SO envelope. (*Bottom row*) PV cuts along to the jet axis. Solid, dashed, and dot-dashed curves are derived assuming a free-fall motion $v_r = -v_{r0}(R/R_0)^{-1/2}$, with $v_{r0} = 2.4, 1.9,$ and $1.5,$ respectively. The contours start at 2σ and have a step of 2σ , where $\sigma = 0.2 \text{ Jy beam}^{-1}$ for C^{18}O and SO and $\sigma = 0.4 \text{ Jy beam}^{-1}$ for ^{13}CO .

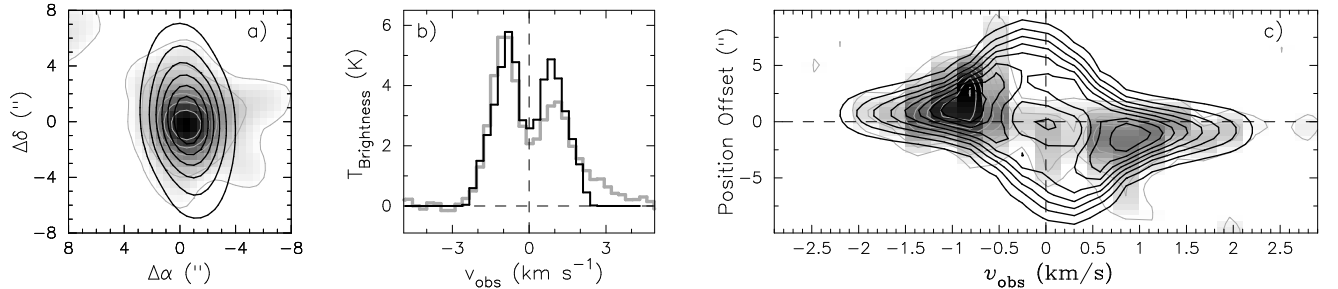


Fig. 6.— A simple model fitting to the C^{18}O emission, spectrum, and PV diagram cut perpendicular to the jet axis. See the text for model description. Black contours and spectrum are from model.